# High quality strained InGaAsP/InGaAsP/InP multiquantum well lasers for 1.55$\mu$m emission grown by MOVPE

M.T. Furtado, W. Carvalho Jr., A.A. Bernussi and A.L. Gobbi

*Laboratório de Optoeletrônica,*

*Fundação CPqD/LNLS-ABTLuS,*

*CP 6070, Campinas, 13083-970, SP*

Recebido 30 de novembro 1998

Strained layer multiquantum well (SL-MQW) lasers incorporating an InGaAsP/ InGaAsP/ InP heterostructure for 1.55 $\mu$m emission wavelength, were grown by low pressure metalorganic vapor phase epitaxy (LP-MOVPE). The SL-MQW heterostructures contained either 5 or 7 quaternary QW layers grown under +0.5% or +1% compressive strain between lattice matched quaternary barriers. Zero net strain (ZNS) heterostructures consisting of 10 compressive QWs grown under +1% strain between tensile strained barrier layers with an equal and opposite strain-thickness product, were also investigated. The laser devices were processed with broad area stripes and ridge waveguide (RWG) structures. The threshold current density at infinite cavity length per well decreased from 150 to 87A/cm with increasing strain in compressive SL-MQW lasers. The corresponding value measured on ZNS-MQW lasers was 102A/cm$^2$. The absorption losses increased with the number of QWs, but were found to be always in the range of 1 to 3.6cm$^{-1}$ per well for both device structures. RWG lasers 300$\mu$m long exhibited the best performances with compressively SL-MQW heterostructures containing 7 QWs grown under +1% strain. The threshold currents and slope efficiencies measured in these devices were between 18-21mA and 0.21-0.26mW/mA per facet, respectively. The excellent uniformity of electro-optic characteristics measured on RWG lasers demonstrates good control of the fabrication process of the ridge mesas.

Heteroestruturas de InGaAsP/InGaAsP/InP constituídas de múltiplos poços quânticos tensionados (SL-MQW), foram crescidas por epitaxia metalorganica em fase vapor a baixa pressão (LP-MOVPE), visando a fabricação de dispositivos lasers para emissão em 1.55$\mu$m. As heteroestruturas tensionadas SL-MQW contêm 5 ou 7 poços quânticos de material quaternário crescidos sob compressão biaxial de +0.5% ou +1%. entre barreiras quaternárias casadas com o InP. Heteroestruturas com tensão total nula (ZNS), constituídas de 10 poços quânticos crescidos sob compressão biaxial de +1% e barreiras sob dilatação biaxial, cujo produto tensão-espessura é igual e oposto ao dos poços, também foram investigadas. Os dispositivos lasers foram processados com estrutura de área larga e guiamento "ridge" (RWG). A densidade de corrente limiar extrapolada para cavidade infinita por poço quântico, diminui de 150 a 87A/cm$^2$ quando a compressão biaxial aumenta em lasers SL-MQW. O valor correspondente medido em lasers ZNS-MQW é de 102A/cm$^2$. As perdas por absorção aumentam com o número de poços, mas situam-se sempre na faixa de 1 a 3.6 cm$^{-1}$ nas duas estruturas de dispositivos. Lasers RWG de 300$\mu$m de comprimento de cavidade, apresentaram melhor desempenho com heteroestruturas tensionadas SL-MQW de 7 poços crescidos sob compressão biaxial de +1%. A corrente limiar e a eficiência diferencial nesses dispositivos estão na faixa de 18-21mA e 0.21-0.26mW/mA por face, respectivamente. A excelente uniformidade das características eletro-ópticas medidas nos lasers RWG, demonstra o bom controle obtido no processo de fabricação da estrutura "ridge".

# I Introduction

The great improvement of semiconductor laser performance reported in recent years, is largely due to the advent of strained layer multiquantum well (SL-MQW) heterostructures. The difference in lattice parameter between the strained QW layer and the substrate results in a biaxial strain perpendicular to the growth direction. The strain produces a tetragonal distortion of the crystal lattice, which lifts the degeneracy of the heavy hole and the light hole subbands in the valence band [1]. Under biaxial compression, the top of the valence band is light hole-like in the in-plane direction, such that the low effective mass of the hole reduces the areal carrier density necessary to achieve the population inversion in a QW laser. Therefore, the current density at transparency is lower in a compressively strained QW laser than in an unstrained one. In addition, the splitting of the spin orbit split-off hole subband in long wavelength lasers is modified in such a way, that only large momentum wavevectors are possible in the transitions involving Auger nonradiative recombination and intervalence band absorption (IBVA) losses. These in turn reduce the threshold current density and increase the external differential efficiency of 1.55$\mu$m emission QW lasers. Hence. devices fabricated with compressively SL-MQW heterostructures have exhibited superior performances when compared to unstrained QW devices [2,3].

However, there is a limit to the total amount of strain that can be incorporated in a SL-MQW structure without the formation of misfit dislocations, which can degrade the laser performance and reliability. Moreover, the growth of SL-MQW structures with more wells can improve the dynamic properties of laser devices in the 1.55$\mu$m wavelength range. A greater number of wells decreases the threshold gain, and therefore increases the differential gain of a MQW laser device. This in turn improves the frequency response and reduces the wavelength chirp, which are important dynamic characteristics for applications in high speed and long distance optical communications. Consequently, there has been a growing interest recently, in strain compensated MQW structures, where the barriers are grown under tensile strain. The strain-thickness product of the barriers is made equal in magnitude but of opposite sign to that of the wells, leading to a structure with zero net strain (ZNS). Strain compensated SL-MQW lasers using the InGaAs(P)/InP system in the range of 1.55$\mu$m emission wavelength have demonstrated excellent electro-optic characteristics [4-7]. An important aspect for the design of ZNS-MQW lasers, is the possibility of growing quaternary wells with larger thickness, which increase the optical confinement factor as well as the allowed tolerances of well thickness and interface sharpness. However, the growth of a greater number of quaternary wells in ZNS-MQW lasers has been limited by a phenomenon known as wavy layer growth, produced mainly by the miscibility gap of the quaternary material usually grown for the tensile strained barrier layers [8,9].

In a recent work, we have reported a systematic study of the growth conditions of metalorganic vapor phase epitaxy (MOVPE), for the improvement of structural and optical properties of InGaAsP/InGaAsP/InP ZNS-MQW heterostructures with a larger number of QWs [10]. In the present work, we present the fabrication of SL-MQW lasers with 1.55$\mu$m wavelength emission which incorporate quaternary InGaAsP materials for the wells and barriers. Compressive SL-MQW lasers with 5 and 7 wells as well as ZNS-MQW lasers with 10 wells were fabricated. The laser devices were processed with broad area stripes and using the ridge waveguide (RWG) structure. Excellent device characteristics were obtained for both SL-MQW structures with lattice mismatches of the QW layers of 0.5% and 1%. The paper is organized as follows: in section II, we describe the epitaxial growth procedure and the processing undertaken for device fabrication. Section III presents results obtained for the material characterization of the SL-MQW heterostructures. Section IV is devoted to the analysis of broad area lasers in order to extract the relevant material and device parameters of compressive SL-MQW lasers and ZNS-MQW laser structures. In section V, we describe the characteristics obtained for the RWG lasers, and finally in section VI, the conclusion is presented.

# II Epitaxial growth and device fabrication

The samples were grown in a horizontal low pressure (70 Torr) MOVPE reactor operating at 670°C growth temperature, using a fast vent-run switching mani-

fold to achieve abrupt heterointerfaces. The group V hidrides sources are phosphine ($PH_3$) and arsine ($AsH_3$), whereas the group III organometalic sources are trimethylindium (TMI) and triethylgallium (TEG). Disilane ($Si_2H_6$) and diethylzinc (DEZn) are used for $n$ and $p$ type doping, respectively. The SL-MQW laser structures comprised the growth of the following successive layers on a $n^+$-InP substrate: 1) a 0.5 $\mu$m thick $n$-type InP buffer layer ($n = 7 \times 10^{17}$ cm$^{-3}$), 2) an undoped active region consisting of a separate confinement heterostructure, which incorporates the SL-MQW structure sandwiched between two waveguide layers of InGaAsP material described below, 3) a 1.8$\mu$m thick $p$-type InP confining layer ($p = 7 \times 10^{17}$ cm$^{-3}$), and 4) a 0.15-0.3 $\mu$m thick $p^+$-InGaAs contact layer ($p > 10^{19}$ cm$^{-3}$). The SL-MQW structures consist of compressively strained QW layers 50 Å thick of InGaAsP material with bandgap wavelength of 1.65$\mu$m, and barrier layers 100 Å thick of InGaAsP material either grown lattice matched or under tensile strain with a corresponding bandgap wavelength of 1.3$\mu$m and 1.4$\mu$m, respectively. The waveguide layers of quaternary material have the same composition as the barriers. The compressive SL-MQW structures included 5 or 7 QW layers between quaternary lattice matched barriers and waveguide layers 500 Å thick. The amount of strain ($\epsilon$) in the QW quaternary layers was nominally +0.5% or +1%. One sample with 5 QWs and $\epsilon$ = +0.5% was grown with waveguide layers 1000 Å thick. The ZNS-MQW structure includes 10 compressively strained QW layers ($\epsilon$ = +1%) 50 Å thick of quaternary material grown between tensilely strained barrier and waveguide quaternary layers ($\epsilon$=-0.5%) 100 Å thick.

Broad area lasers were processed into stripes of 50 and 100 $\mu$m widths using a conventional photolithography technique. The fabrication of the RWG structure included a combination of reactive ion etching (RIE) and wet chemical etching techniques with a photoresist mask. The ridge mesas of 5$\mu$m width were etched through the $p^+$-InGaAs contact layer and the $p$-InP confinement layer down to the upper quaternary waveguide layer. $SiO_2$ was deposited by PECVD to confine the current in the active region only below the ridge. The $p$ side contacts of the broad area stripes and on top of the ridge mesas were performed by evaporation of Ti/Pt/Au. After thinning the substrates down to 100$\mu$m thickness, the $n$ side ohmic contact was formed by deposition of Ni/AuGe/Ni/Au by electron beam. The laser devices were obtained after cleaving the wafer into bars of various cavity lengths in the range 240-1200$\mu$m. Finally, the light output power-current characteristics were measured at room temperature under pulsed conditions at a frequency of 1KHz with current pulses of 1$\mu$s width.

## III Material characterization

After growth, the SL-MQW structures were characterized by double crystal X-ray diffraction and photoluminescence (PL) spectroscopy techniques. Fig. 1 presents the X-ray rocking curve of a SL-MQW structure grown with 7 compressively strained QW layers ($\epsilon$=+0.5%). The zero order diffraction peak yields a resultant compressive lattice mismatch equal to $3.42 \times 10^{-3}$. The separation between the higher order satellite peaks yields a 168 Å period for the sum of the QW and barrier layers, which is close to the nominal value. The PL spectrum measured on this sample at room temperature is shown in Fig. 2. The relatively narrow emission peak at 1.565$\mu$m is close to the expected value and reveals good reproducibility of the 7 QW layers in this compressive SL-MQW structure. The high intensity and uniform PL emission measured on different parts of the sample confirm the good quality of the as-grown material. Similar results were obtained with compressive SL-MQW structures grown with $\epsilon$=+1%, and also grown with 5 QWs.

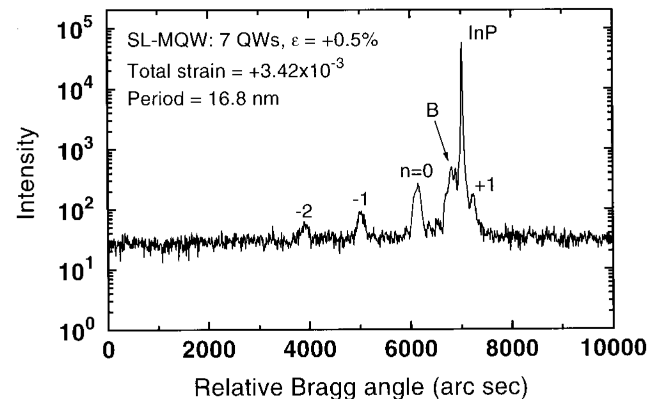


Figure 1. X-ray rocking curve of a SL-MQW heterostructure grown with 7 QWs under compressive strain ($\epsilon$=+0.5%) measured at (400) reflection. Peaks B and InP refer to the waveguide quaternary layers and the substrate, respectively.

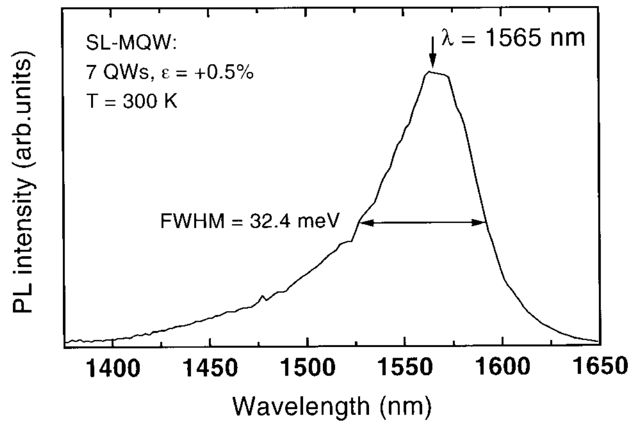


Figure 2. PL spectrum measured at room temperature of a SL-MQW heterostructure grown with 7 QWs under compressive strain ($\epsilon$=+0.5%). FWHM is the full width at half maximum of the PL peak.

The X-ray rocking curve measured on a ZNS-MQW structure is shown on Fig. 3. The more intense, sharper and higher order satellite peaks, as compared to the SL-MQW sample of Fig.1, result from the greater material volume available for X-ray diffraction due to the larger number of QWs and barriers in this MQW structure. The zero order peak slightly shifted towards the tensile strained material presents a resultant lattice mismatch equal to $-6\times10^{-4}$. The separation of the satellite peaks yields a 125Å period for the sum of the QW and barrier layers. The corresponding PL spectrum is shown in Fig. 4, where the peak emission is somewhat shifted to lower wavelengths relative to the nominal value. The simulated X-ray rocking curve shown in Fig. 3 was performed assuming the nominal strain values for the well and barrier layers. The corresponding bandgap compositions were deduced from the PL peak position and the resultant strain measured by X-ray diffraction. The simulation reveals good periodicity for wells and barrier layers with thicknesses of 47 Å and 79 Å, respectively, somewhat smaller than the nominal values, but in agreement with the shift observed in the PL spectrum. The scatter in thickness relative to the nominal values observed for the SL-MQW and the ZNS-MQW structures, result from uncertainties in the calibration procedure of the composition and thickness of the quaternary layers for the wells and barriers. In fact, both parameters were adjusted for the growth of each MQW heterostructure in order to obtain the PL peak emission as close as possible to 1.55$\mu$m wavelength.

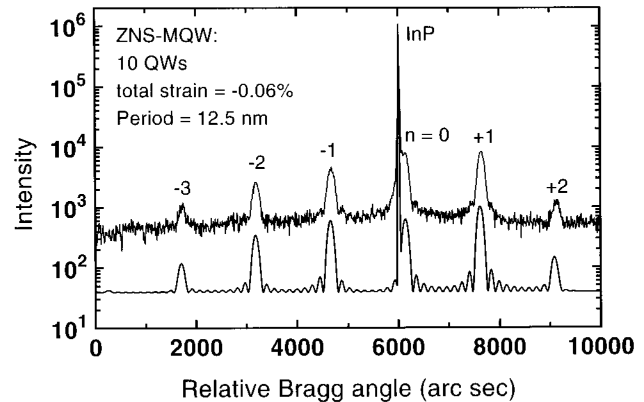


Figure 3. X-ray rocking curve of a ZNS-MQW heterostructure grown with 10 QWs under compressive strain ($\epsilon$=+1%) and barriers under tensile strain ($\epsilon$=-0.5%), measured at (400) reflection.

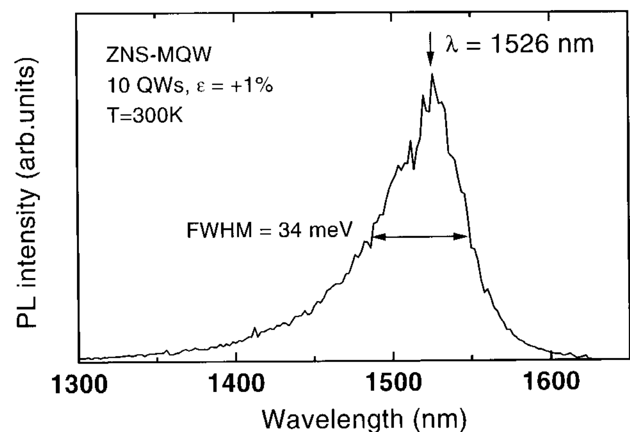


Figure 4. PL spectrum measured at room temperature of a ZNS-MQW heterostructure grown with 10 QWs under compressive strain ($\epsilon$=+1%) and barriers under tensile strain ($\epsilon$=-0.5%).

## IV Broad area lasers analysis

The light-current characteristics of compressive SL-MQW broad area lasers grown with $\epsilon$ = +0.5% and +1% and cleaved with different cavity lengths, are presented in Figs. 5 and 6, respectively. On both figures, one clearly observes the expected increase of the threshold current with the concomitant decrease of the slope efficiency, as the cavity length is increased. However, by comparing devices cleaved with the same cavity length, but grown with different strains, one notices a threshold current decrease and a slope efficiency increase as the strain increases. These observations are consistent with the prediction of the reduction of losses due to Auger recombination and IBVA transitions. produced by the

modified valence band structure of the quaternary material in the QW layers in the presence of compressive strain [1,2].

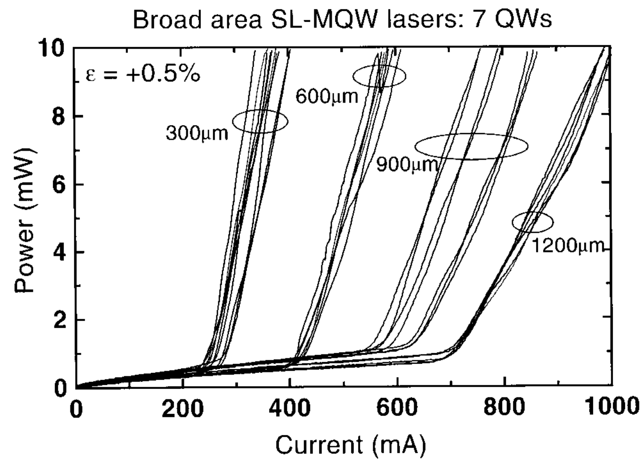


Figure 5. Output power-current characteristics of broad area lasers of various cavity lengths for a SL-MQW heterostructure grown with 7 QWs under compressive strain ($\epsilon$=+0.5%).

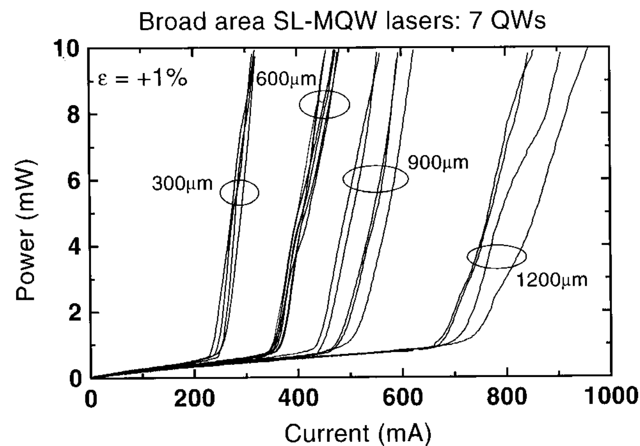


Figure 6. Output power-current characteristics of broad area lasers of various cavity lengths for a SL-MQW heterostructure grown with 7 QWs under compressive strain ($\epsilon$=+ 1 %).

Figs. 7, 8 and 9 present plots of the threshold current density ($J_{th}$) as a function of inverse cavity length ($L$) and the reciprocal differential quantum efficiency ($\eta_{ext}$) versus $L$ for three samples. Figs. 7 and 8 show measured data on compressive SL-MQW structures: the former grown with $\epsilon$ = 0.5% and 5 QWs, and the latter with $\epsilon$ = 1% and 7 QWs. Fig. 9 shows plots of the ZNS-MQW laser structure grown with 10 QWs. The straight lines in these figures are least square fits of the experimental data points. Notice the large number of devices measured for the ZNS structure and the excellent uniformity of threshold current densities obtained. In the following, we describe the modeling analysis undertaken to describe the experimental data shown in these figures. A major difference with previous works, is the large number of lasers analyzed here which are represented by least square fits, and not only data measured from best devices.

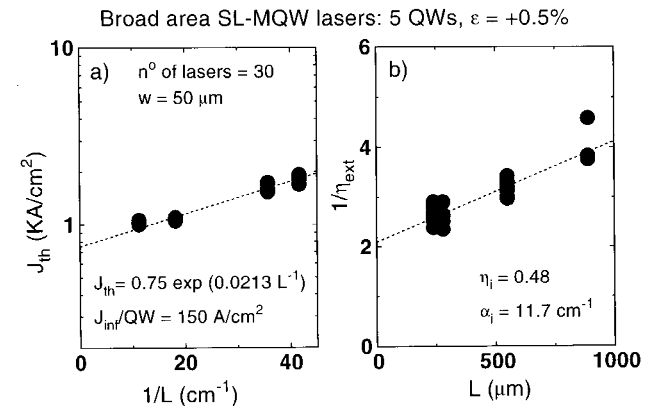


Figure 7. Plots of the threshold current density as a function of inverse cavity length (a) and the reciprocal external differential efficiency versus cavity length (b) measured on broad area lasers for a SL-MQW heterostructure grown with 5 compressively strained QWs ($\epsilon$=+0.5%). The broad area stripe width (w) and the number of lasers measured are also indicated.

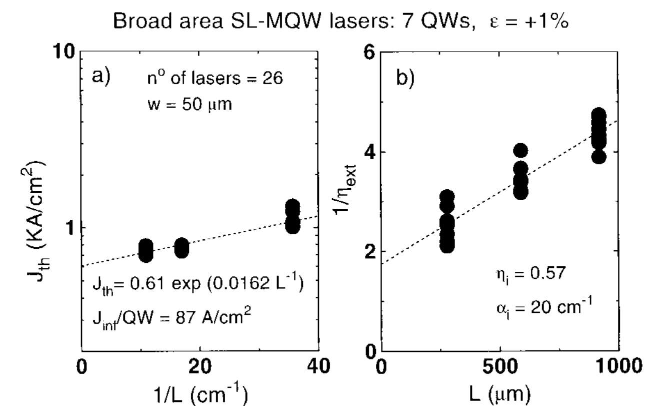


Figure 8. Plots of the threshold current density as a function of inverse cavity length (a) and the reciprocal external differential efficiency versus cavity length (b) measured on broad area lasers for a SL-MQW heterostructure grown with 7 compressively strained QW layers ($\epsilon$=+1%).

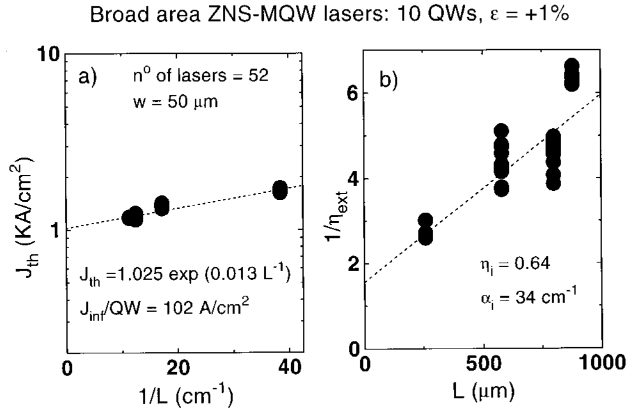


Figure 9. Plots of the threshold current density as a function of inverse cavity length (a) and the reciprocal external differential efficiency versus cavity length (b) measured on broad area lasers for a ZNS-MQW heterostructure. The 10 QWs are grown compressively strained ($\epsilon$=+1%) between barriers under tensile strain ($\epsilon$=-0.5%) of double thickness.

The exponential behavior observed in the plots of the threshold current density versus $1/L$ is a direct consequence of the logarithmic dependence of the material optical gain with the current density $J$ in a single QW layer, which is given by the expression [11]:

$$G = G_0 \ln \frac{\eta_i J}{J_0} \tag{1}$$

where $G_0$ is the gain coefficient, $J_0$ is the current density at transparency and $\eta_i$ is the injection efficiency. The current density can be assumed equally divided among the different QWs. Assuming the laser threshold condition, where the gain equals the absorption and mirror losses in conjunction with equation (1), the exponential expression of $J_{th}$, as a function of $1/L$ in a MQW laser is easily obtained [12]

$$J_{th} = J_{inf} \exp\left(\frac{Y}{L}\right) \tag{2}$$

The threshold current at infinite cavity length $J_{inf}$ and the parameter $Y$ are given by:

$$J_{inf} = \frac{N_z J_0}{\eta_i} \exp\left(\frac{\alpha_i}{, G_0}\right) \tag{3}$$

$$Y = \frac{1}{, G_0} \ln \frac{1}{R} \tag{4}$$

where , is the optical confinement factor of the MQW structure, $\alpha_i$ is the internal absorption loss, $N_z$ is the number of QWs and $R$ is the facet reflectivity. The value of $J_{inf}$ is given by the intercept at the ordinate of the fit line on the plot of $J_{th}$ versus $1/L$ using equation (2). The threshold current density at infinite cavity length per well $J_{inf}/QW$, is an important parameter commonly used to characterize the optical and crystalline quality of SL-MQW lasers [2]. From Figs. 7a and 8a, we find $J_{inf}/QW$ = 150 A/cm$^2$ and 86.8 A/cm$^2$ for the compressive SL-MQW lasers grown with $\epsilon$ = +0.5% and $\epsilon$ = +1%, respectively. These results are comparable to data previously reported on similar compressive SL-MQW laser structures which operate around 1.55$\mu$m emission [2,13,14], and they follow the expected trend with increasing amount of strain. As the compressive strain in the QW layer increases, the hole effective mass decreases and the splitting between the heavy and light hole subbands increases. Both effects contribute to the observed reduction of $J_{inf}/QW$ with increasing compressive strain. However, we should point out that most previous works reported on compressive SL-MQW lasers employed ternary InGaAs QWs [2]. Moreover, the results reported with quaternary QWs were obtained in laser structures grown with lower number of QWs [3,13,14] or lower strain values [15].

Following the same analysis presented above, we find $J_{inf}/QW$ = 102 A/cm$^2$ from the data shown in Fig. 9a for the ZNS structure. There is less available data reported on $J_{inf}/QW$ in ZNS structures with 1.55$\mu$m emission. A lower value of 62A/cm$^2$ was recently reported in a strain compensated quaternary structure with 10 QWs [15], but grown with lower compensation than our samples, since their strain in the wells and barriers were +0.64% and -0.17%, respectively. Other results were reported employing ternary InGaAs QWs [5] as well as a lower number of quaternary QWs [6,16]. The $J_{inf}/QW$ values obtained are somewhat lower than ours. One possible reason for this discrepancy, are inhomogeneities in the MQW layers that might be related to wavy layer growth in ZNS quaternary structures, which are known to increase with the number of QWs [8-10]. However, the value reported for a ZNS AlGaInAs/AlGaInAs structure grown with 10 QWs [17] is significantly higher than ours. This result is surprising since the growth of AlGaInAs MQW structures usually have more flat interfaces.

In addition, we have determined the gain coefficient using the value of the semilogarithmic slope $Y$ obtained from the plot of the threshold current density versus $1/L$ given by equation (2). The calculation of the optical confinement factor of the SL-MQW laser structures of Figs. 7a and 8a, yields the values of , = 0.0437 and 0.0718, respectively. The higher value of the latter sample results from the corresponding larger number of QWs. Therefore, assuming $R$ = 0.3 in the expression of $Y$ given in equation (4), we find $G_o$ = 1329 cm$^{-1}$

and 1034 cm$^{-1}$ for the samples shown in Figs. 7a and 8a. respectively. These results are consistent with data reported previously on similar SL-MQW lasers [3,18]. However, the decrease of $G_o$ observed in the SL-MQW sample grown with higher strain ($\epsilon = +1\%$) is inconsistent with the increase of the number of QWs as well as the amount of strain. A possible explanation for this unexpected behavior might be the existence of inhomogeneities among the QW layers, which increase in the growth direction and consequently reduce the material gain. On the other hand, following the same analysis for the ZNS structure and assuming , = 0.0937, we find $G_o$ = 989 cm$^{-1}$. This value is lower than those measured in compressive SL-MQW structures having a smaller number of QWs. Possible inhomogeneities in the QW layers related to the onset of wavy layer growth in the ZNS structure might be responsible for the reduction of the gain in this case.

The values of $\alpha_i$ and $\eta_i$ were obtained from the plots of $1/\eta_{ext}$, versus $L$ using the well known expression [2]:

$$\frac{1}{\eta_{ext}} = \frac{1}{\eta_i}\left(1 + \frac{\alpha_i L}{\ln\frac{1}{R}}\right) \qquad (5)$$

With equation (5) and the best fit lines of $1/\eta_{ext}$ as a function of $L$ shown in Figs. 7b and 8b, we obtain the values: $\alpha_i = 11.7$ cm$^{-1}$ and $\eta_i = 0.48$ for the SL-MQW with $\epsilon = +0.5\%$, and $\alpha_i = 20$ cm$^{-1}$ and $\eta = 0.57$ for the SL-MQW with $\epsilon = +1\%$. From the best fit line of the ZNS structure shown in Fig. 9b, we find the values $\eta_i = 0.64$ and $\alpha_i = 34$ cm$^{-1}$ using equation (5). One notices a significant increase of the internal losses with the strain as well as with the number of wells. The internal losses per well $\alpha_i/QW$ of these samples correspond to the values 2.3, 2.9 and 3.4 cm$^{-1}$ for the compressive SL-MQW structures grown with $\epsilon = +0.5\%$, $\epsilon = +1\%$ and the ZNS structure, respectively. These results can be considered quite close compared to more scattered data reported with similar ZNS-MQW structures [19]. Our results show that the losses are mainly affected by the number of QW layers in these structures. In a previous work, $\alpha_i$ was observed to be independent of $N_z$ and decreased with increasing amount of compressive strain [3]. This discrepancy may be attributed to scattering losses in the QW interfaces due to the larger number of QWs used in this work, such that $\alpha_i$ is not only limited by the IVBA losses. However, we must point out that the value of $\alpha_i$ measured in our ZNS structure is significantly lower than the value reported recently [19] for a similar structure with the same number of QWs.

Table I presents data gathered from various SL-MQW structures grown with different strains and number of QWs. The lasers were processed with stripe widths of 50$\mu$m where not specified. One notices a decrease of $J_{inf}/QW$ values by a factor around 22-28% on the same sample when the stripe width increases from 50 to 100$\mu$m. This behavior is explained by the contribution of current spreading below the broad area stripe, which are known to increase as the stripe width decreases. This result implies that the values measured for the compresslve SL-MQW structure with $\epsilon$=+1% and the ZNS structure are possibly overestimated by the same amount. On the other hand, the low values of $\eta_i$ measured on lasers processed with the larger broad area stripe may be attributed to an inhomogeneous distribution of the carrier density below the stripe. In a previous work [20], we have shown that this effect does not affect the value measured of $\alpha_i$. Finally, the values shown for the current density at transparency $J_0$ were determined using equation (3) with known values of $J_{inf}$, $G_o$ and $\alpha_i$ obtained from equations (2), (4) and (5), respectively. The results are consistent with data previously reported [3,21], and are among the best results obtained on similar SL-MQW structures. As expected, $J_o$ decreases as the compressive strain increases in the QW layer, due to the decrease of the hole effective mass in the valence band. However, the decrease of $J_o$ observed with increasing stripe width on the same sample, results from the corresponding lower value measured of $\eta_i$.

Table I: Laser characteristics of compressively SL-MQW and ZNS-MQW structures

| Sample | $\varepsilon$ (%) | n° of wells | n° of lasers | $J_{inf}$ (A/cm$^2$) | $Y$ (cm) $\times 10^{-2}$ | $J_{inf}$/QW (A/cm$^2$) | $\Gamma$ $\times 10^{-2}$ | $G_0$ (cm$^{-1}$) | $\eta_i$ | $\alpha_i$ (cm$^{-1}$) | $\alpha_i$/QW (cm$^{-1}$) | $J_0$ (A/cm$^2$) |
|---|---|---|---|---|---|---|---|---|---|---|---|---|
| B467 | +0.5% | 7 | 35 | 1031 | 1.6 | 147 | 7.8 | 967 | - | - | - | - |
| B469 | +1% | 7 | 19 | 932 | 1.41 | 132 | 7.18 | 1186 | - | - | - | - |
| B485 | +0.5% | 5 | 30 | 752 | 2.13 | 150 | 4.37 | 1295 | 0.48 | 11.7 | 2.3 | 58.6 |
| B485 (100μm) | +0.5% | 5 | 12 | 587 | 2.3 | 117 | 4.37 | 1200 | 0.4 | 5 | 1 | 42.5 |
| B486 | +0.5% | 5 | 17 | 762 | 2.07 | 152 | 4.37 | 1329 | 0.49 | 8.5 | 1.7 | 64.3 |
| B486 (100μm) | +0.5% | 5 | 7 | 546 | 2.54 | 109 | 4.37 | 1085 | 0.44 | 6.2 | 1.2 | 42.1 |
| B486 (RWG) | +0.5% | 5 | 50 | 891 | 1.42 | 178 | 4.37 | 1937 | 0.67 | 13 | 2.6 | 102.3 |
| B487 | +1% | 7 | 26 | 608 | 1.62 | 87 | 7.18 | 1034 | 0.57 | 20 | 2.9 | 37.9 |
| B531 | ZNS | 10 | 52 | 1025 | 1.3 | 102 | 9.37 | 989 | 0.64 | 34 | 3.4 | 45.2 |
| B531 (RWG) | ZNS | 10 | 47 | 1189 | 0.997 | 119 | 9.37 | 1289 | 0.78 | 34 | 3.4 | 70 |
| B553 | +0.5% | 5 | 91 | 606 | 2.51 | 121 | 4.37 | 1097 | 0.52 | 17.8 | 3.6 | 43.5 |

# V RWG lasers

The light output power-current characteristics measured on compressively SL-MQW RWG lasers grown with 7 QWs and $\epsilon$=+1%, cleaved with 300 $\mu$m cavity length, are shown in Fig. 10. The devices present very uniform characteristics and operate with low threshold currents and high slope efficiencies in the ranges of 18 - 21mA and 0.21-0.26mW/mA per facet, respectively. These results are among the best reported for compressive strained MQW RWG lasers in the range of 1.55$\mu$m emission wavelength [22-24]. Similar laser characteristics with excellent uniformity along the wafer were also measured on compressive SL-MQW lasers grown with 5 QWs and $\epsilon$=+0.5% as well as on ZNS structure lasers grown with 10 QWs, with both structures cleaved with various lengths. Plots of the threshold current density and the differential efficiency as a function of cavity length for the ZNS structure are shown in Fig. 11 for 50 laser devices. The device parameters extracted from these plots and other similar plots for the compressive SL-MQW structures are presented in Table I. One notices a close similarity with the corresponding values measured on broad area lasers from the same wafer, although the values of $J_{inf}/QW$ are somewhat higher in RWG laser structures. This discrepancy can be attributed to the existence of a lateral diffusion current in the RWG structure that occurs through the QW and the waveguide layers, which has been shown to increase with the cavity length [25]. Hence, the values measured of $J_{th}$ are somewhat higher for RWG lasers of longer cavity lengths, and the values measured of $J_{inf}/QW$ and $G_o$ exhibit an apparent increase. On the other hand, the absorption loss of RWG lasers shown in Table I, increases for the compressive SL-MQW structure grown with $\epsilon$=+5%, but remains unchanged for the ZNS structure. The former result indicates that additional scattering losses, probably related to roughness of the ridge sidewalls, were introduced by the processing steps involved in the fabrication of the ridge mesas. However, these losses are not significant since such RWG lasers operate with a low threshold current and a high differential efficiency as shown above. Besides, the unchanged behavior of the absorption loss in the ZNS structure, shows that the processed ridge mesas in the present work are of excellent quality when performed under optimal conditions. It should be pointed out that our ridge mesas are about twice wider than those reported in most previous works, and the number of wells in both compressive SL-MQW and ZNS-MQW RWG laser structures is also higher. This explains the higher threshold currents measured in this work when compared to some previous reports on similar SL-MQW RWG lasers [22-24].

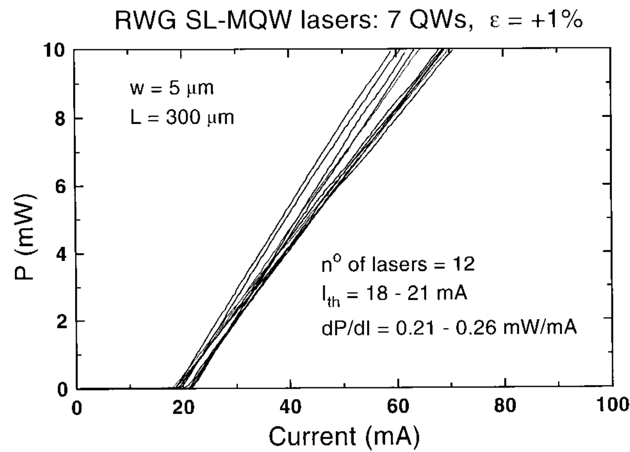


Figure 10. Output power-current characteristics of RWG lasers cleaved with 300$\mu$m cavity lengths. The SL-MQW heterostructure was grown with 7 compressively strained QWs ($\epsilon$=+1%). $I_{th}$ and $dP/dI$ represent the measured threshold currents and slope efficiencies, respectively. The ridge mesa stripe width (w) and the number of lasers measured are also indicated.

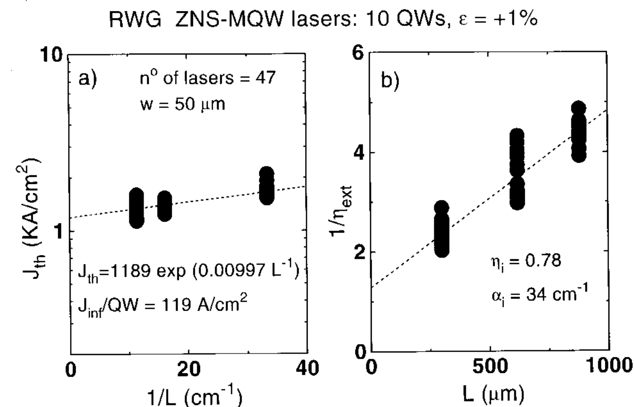


Figure 11. Threshold current density (a) and external differential efficiency (b) measured on RWG lasers plotted as a function of cavity length for a ZNS-MQW heterostructure. The 10 QWs are grown compressively strained ($\epsilon$=+1%) between barriers under tensile strain ($\epsilon$=-0.5%) with double thicknesses.

# VI Conclusion

We have successfully grown compressive and ZNS InGaAsP/InGaAsP/InP SL-MQW lasers heterostructures by low pressure MOVPE for 1.55$\mu$m emission wavelength. The characterization by X-ray diffraction and PL analysis demonstrate an excellent structural and optical quality of the quaternary materials in the heterostructures grown for the laser devices. Broad area stripe and RWG structure lasers exhibited excellent electro-optical characteristics with low threshold current densities, high differential efficiencies and low internal losses. As the strain increases in compressive SL-MQW lasers, the threshold current density decreases and the slope efficiency increases, in agreement with predictions expected by the strain increase in the valence band structure of the QW material. The low threshold current at infinite cavity length measured on compressively SL-MQW lasers grown with 7 QWs and $\epsilon$=1% as well as in ZNS-MQW lasers are among the best obtained in similar structures with the same number of quaternary wells. In addition, the absorption losses per well remained very low, although they increased somewhat with the number of wells, possibly due to the corresponding increase of inhomogeneities along the growth direction. Finally, the RWG laser electro-optical characteristics are comparable to the best results obtained in recent works. The good uniformity of laser characteristics and the small incremental losses of the RWG structure, demonstrate good control of the fabrication process of the ridge mesas in this work.

## Acknowledgements

The authors would like to thank H.,Gazetta Filho and L.C. Silveira Vieira for technical assistance in material growth, X-ray measurements and device processing. We also acknowledge stimulating discussions with S.D. Perrin from British Telecom Laboratories during the initial part of this work.

# References

1. E.P.O'Reilly and A.R. Adams, IEEE J. Quantum Electron. **30**, 366 (1994).
2. P.J.A. Thijs, L.F. Tiemeijer, J.J.M. Binsma and T.V. Dongen, IEEE J. Quantum Electron. **30**, 477 (1994).
3. J.S. Osinski, P. Grodzinski, Y. Zou and P.D. Dapkus, IEEE J. Quantum Electron. **29**, 1576 (1993).
4. C.P. Seltzer, S.D. Perrin, M.C. Tatham and D.M. Cooper, Electron. Lett. **28**, 63 (1992).
5. A.T.R. Briggs, P.D. Greene and J.M. Jowet, IEEE Photon. Technol. Lett. **4**, 423 (1992).
6. A. Mircea, A. Ougazzaden, G. Primot and C. Kazmierski, J. Cryst. Growth **124**, 737 (1992).
7. S.D. Perrin, C.P. Seltzer and P.C. Spurdens, J. Electron. Mater. **23**, 81 (1994).
8. U. Bangert, A.J. Harvey, V.A. Wilkinson, C. Dieker, J.M. Jowet. A.D. Smith. S.D. Perrin and C.J. Gibbins, J. Cryst. Growth **132**, 231 (1993).
9. A. Ponchet, A. Rocher. J.Y. Emery, C. Stark and L. Goldstein, J. Appl. Phys. **74**, 3778 (1993).
10. W. Carvalho Jr., A.A. Bernussi, M.T. Furtado, A.L. Gobbi and M.A. Cotta, Materials Research (to be published).

11. T.A. DeTemple and C.M. Herzinger, IEEE J. Quantum Electron. **29**, 1246 (1993).
12. M.T. Furtado, W. Carvalho Jr., C.M.A. Coghi, E.J.T. Manganote and A.C. Bordeaux-Rêgo, Rev. Fís. Apl. Instr., **11**, 142 (1996).
13. J.S. Osinski, Y. Zou, P. Grodinski, A. Mathur and P.D. Dapkus, IEEE Photon. Technol. Lett. **4**, 10 (1992).
14. A. Ougazzaden, A. Mircea, R. Mellet, G. Primot and C. Kazmierski, Electron. Lett. **28**, 1078 (1992).
15. A. Nutch, H. Kratzer, B. Torabi, G. Trankle, G. Abstreiter and G. Wiemann, J. Cryst. Growth **183**, 505 (1998).
16. E. Kuphal, H. Burkhard and A. Porker, Japan. J. Appl. Phys. **34**, 3486 (1995).
17. H. Hillmer, R. Losch, F. Steinhagen, W. Schlapp, A. Pocker and H. Burkard, Electron. Lett. **31**, 1346 (1995).
18. N. Otsuka, M. Kito, M. Ishino and Y. Matsui, IEEE J. Quantum Electron. **32**, 1230 (1996).
19. P.A. Crump, H. Lage, W.S. Ring, R.M. Ash, J. Herniman, S. Wrathall, P.Z.A. DeSouza and A.E. Staton-Bevan, EE Proc. Optoelectron. **145**, 7 (1998).
20. M.T. Furtado, W. Carvalho Jr., A.M. Machado and K. Jomori, Braz. J. Phys. **27**, 456 (1997)
21. A. Mathur and P.D. Dapkus, IEEE J. Quantum Electron. **32**, 222 (1996).
22. A.P. Wright, A.T.R. Briggs, A.D. Smith, R.S. Baulcomb and K.J. Warbrick, Electron. Lett. **29**, 1848 (1993).
23. B. Stegmuller, E. Veuhoff, J. Rieger and H. Hedrich, Electron. Lett. **29**, 1691 (1993).
24. B. Stegmuller, B. Borchert and R. Gessner, IEEE Photon. Technol. Lett. **5**, 597 (1993).
25. S.Y. Hu, D.B. Young, A.C. Gossard and L.A. Coldren. IEEE J. Quantum Electron. **30**, 2245 (1994).